Chapter 5

5.1 Introduction

Previously, in chapter 3 and 4, we have established that after incorporating either 11 at% of Dy or 12 at% of Sm into HfO_2 lattice, one can completely stabilize the high temperature cubic phase at room temperature. This chapter primarily investigates the structure and photoluminescence properties of Dy and Sm codoped HfO_2. In particular, we introduce the concept of stabilizing cubic phase of HfO_2 at room temperature after codoping Dy and Sm. Since 1 at% of Dy or Sm doped HfO_2 demonstrate excellent luminescence properties, *x*Dy,*y*Sm:HfO_2 nanophosphors having low dopant concentrations have been utilized as prospective dusting powder to demonstrate the robustness in developing latent fingerprint (LFPs) for forensic investigations. The developed LFPs onto multivariate object surfaces such as aluminum foil, glass and colored plastic sheets etc exhibit vital details including termination sand bifurcations.

5.2 Results and Discussion

5.2.1 Phase and Structural Transformation of Dy and Sm:HfO_2

In order to investigate the phase transformation in HfO_2 after codoping Dy and Sm, first, *x*Dy,*y*Sm:HfO_2 powders ((*x*=*y*=6); (*x*=6, *y*=7) and (*x*=7, *y*=6)) calcined at 900 ^oC have been characterized by XRD and results are shown in **figure 5.1.** It is evident from XRD patterns that at *x*=*y*=6, along with the intense characteristic diffraction peaks such as (111), (002), (022), (113), and (222) corresponding to the cubic phase, $Fm\bar{3}m$ of HfO_2, a few other peaks at 2θ = 24.6 and 28.3^o appear which are attributed to the monoclinic phase. Because of meager contribution of the monoclinic phase, the cubic phase of HfO_2 prevails

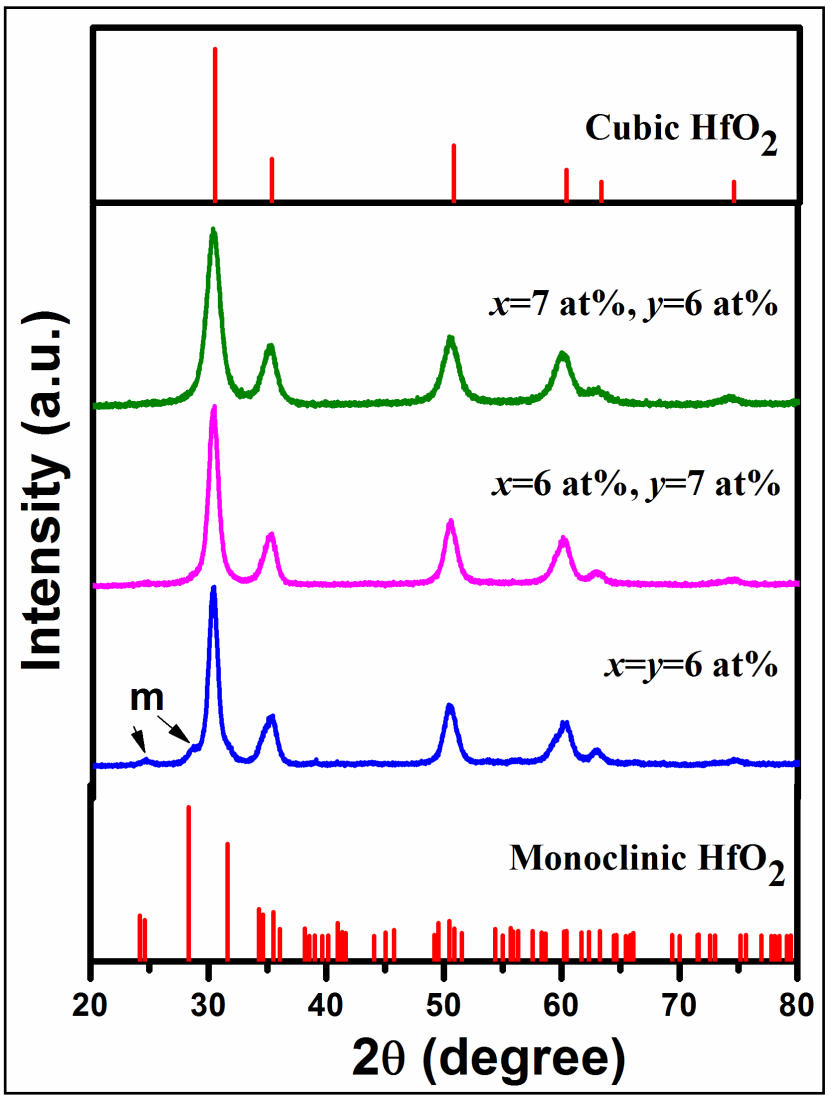

Figure 5.1 *XRD patterns of xDy,ySm:HfO_2powders ((x=y=6); (x=6, y=7) and (x=7, y=6)) calcined at 900 ^oC.*

Dy (*x*), Sm (*y*) (at%)	*x*=0, *y*=0	*x*=0.5, *y*=0	*x*=0, *y*=0.5	*x*=0.5, *y*=0.1	*x*=0.5, *y*=0.3	*x*=0.5, *y*=0.5	*x*=0.5, *y*=1	*x*=0.5, *y*=2
Sample	D0S0	D0.5S0	D0S0.5	D0.5S0.1	D0.5S0.3	D0.5S0.5	D0.5S1	D0.5S2

Table 5.1 *List of synthesized samples with various compositions of xDy,ySm:HfO_2 powders with low dopant concentration.*

in this sample. However, in case of *x*=6, *y*=7 and *x*=7, *y*=6 at%, the monoclinic phase of HfO_2 is completely suppressed and the diffraction peaks corresponding to pure cubic phase are obtained. Therefore, in Dy and Sm codoped HfO_2, it is established that the high temperature cubic phase can be stabilized at RT when Dy and Sm codopant concentration attains 13 at%.

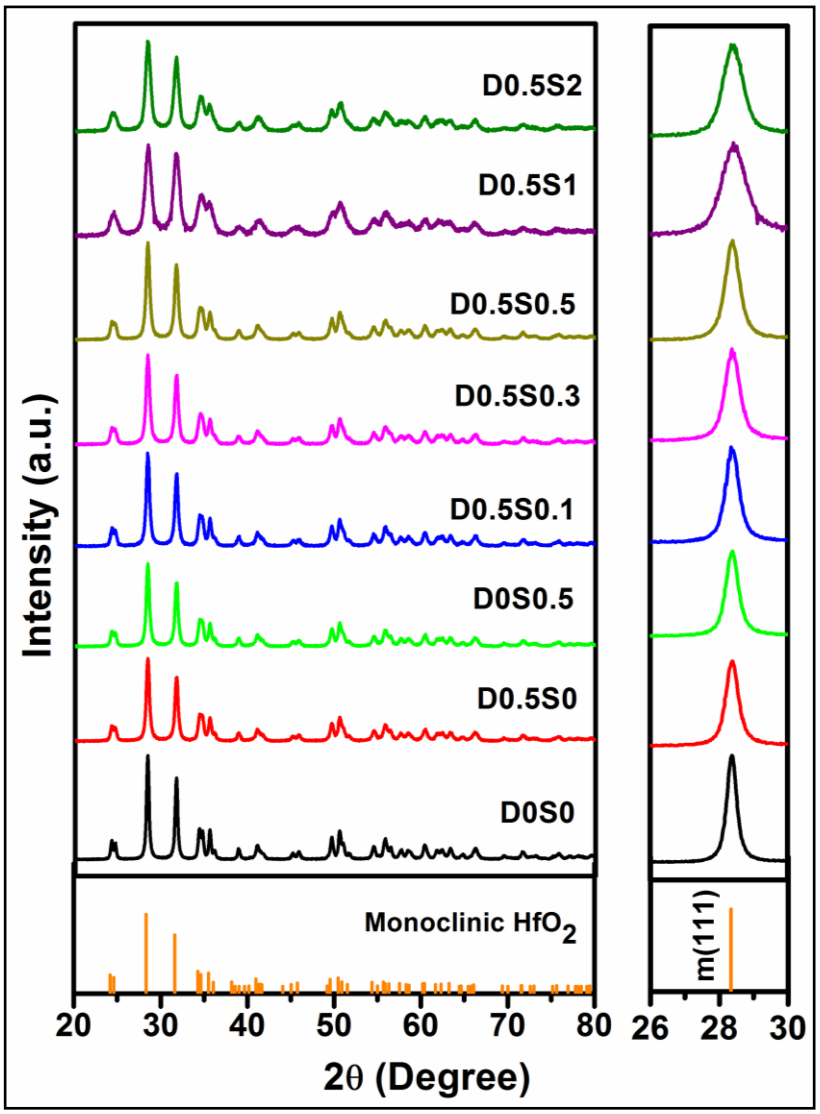

Figure 5.2 *XRD of Dy^{3+} and Sm^{3+} coactivated HfO_2 powders calcined at 900 ^oC (left panel). Right panel indicates broadening of (T11) peak corresponding to monoclinic phase of HfO_2.*

Figure 5.2 depicts the XRD patterns of *x*Dy,*y*Sm:HfO_2 powders with low dopant concentration (listed in **table 5.1**) calcined at 900 °C under ambient conditions. Apparently, XRD patterns exhibit sharp and well resolved diffraction peaks distinctive to crystalline particles. For D0S0, the diffraction peaks are identified as (011), (110), ($\bar{1}$11), (111), (020), (200), (021), ($\bar{2}$11) and (112) of the monoclinic phase, space group, $P2_1/c$ (JCPDS card no. 78-0049) of HfO_2. In D0.5S0.5 sample, one can explicitly note that the intensity of diffraction peaks diminishes noticeably and peaks become broad indicating a significant reduction in crystallite size. While keeping Dy concentration constant at 0.5 at%, increase

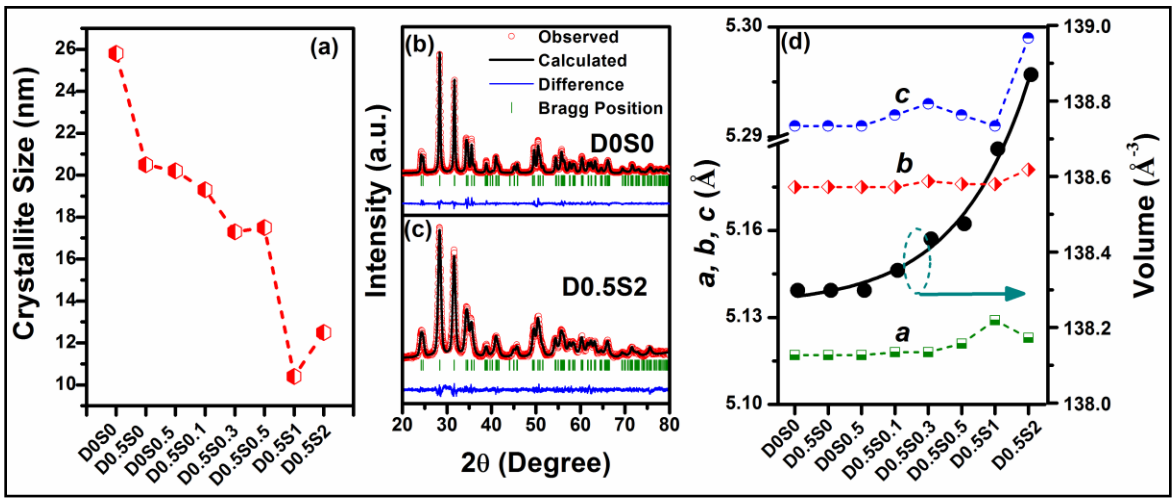

Figure 5.3 (a) *Variation in crystallite size calculated along ($\bar{1}$11) as a function of Dy and Sm concentration; Le-Bail refinement profiles of XRD data of* ***(b)****D0S0* ***(c)*** *D0.5S2 and* ***(d)*** *dependence of lattice constants such as a, b, c and volume upon Dy and Sm concentrations.*

in Sm concentration upto 2 at% indicates broad diffraction peaks demonstrating fine particles. Considering the fact that positions of diffraction peaks remain same, it is noteworthy to mention that incorporation of Sm upto 2 at% in HfO_2 lattice does not change

the crystal structure. The crystallite size of the above compounds is estimated using Debye-Scherrer equation as given below.[162]

$$D = k\lambda/\beta Cos\theta$$

where D is crystallite size, λ is X-ray wavelength, k is constant related to shape of particles, β is full width at half maximum (FWHM in radians) estimated after subtracting instrumental broadening and Kα_2 contributions and θ is the Bragg's angle. The variation in crystallite size calculated along (T11) is shown in **figure 5.3 (a)**. For D0S0, the crystallite size is found to be ~25 nm which substantially decreases to ~20 nm for D0.5S0.5 sample. The crystallite size further reduces to ~10 nm with increasing Sm concentration upto 2 at%. Such a systematic reduction in crystallite size with Sm concentration indicates a higher nucleation rate than the growth rate. It is worth to determine the lattice parameters while the particle size reduces from ~25 to ~10 nm with increase in Sm concentration.

Therefore, XRD patterns are fitted using Le-Bail profile fitting of FULLPROF program with pseudo-Voigt function to refine unit cell parameters such as lattice constants and cell volume. **Figure 5.3 (b) and (c)** shows the typical Le-Bail profile fitting of XRD data with space group, $P2_1/c$ for D0S0 and D0.5S2, respectively. The observed pattern, calculated data after fitting, and the difference pattern between observed and calculated data are shown as open circle, continuous line and as a bottom line, respectively. The vertical tick marks on top of the difference pattern show respective positions of Bragg peaks. All the observed Bragg profiles fit well with monoclinic phase, $P2_1/c$ of HfO_2. The variation in lattice constants and cell volume of *x*Dy,*y*Sm:$HfO_2$with different Sm and Dy concentrations is shown in **figure 5.3 (d)**. One can clearly observe the gradual increment of lattice constants such as '*a'*, '*b'* and '*c'* resulting in enlarged cell volume with increasing Sm

concentrations. While the lattice constant *a* and *b* varies from 5.117 to 5.123 Å and 5.175 to 5.181 Å, respectively, *c* monotonically increases from 5.291 to 5.299 Å. As a result, an exponential expansion of monoclinic cell volume from 138.30 to 138.87 $Å^3$ is observed with increasing Sm concentration. In the monoclinic phase of HfO_2, Hf forms a covalent bond with oxygen and exhibits seven coordinated Hf^{4+} ions.[53, 109] For a 7-fold coordination, the ionic radius of Dy^{3+} (0.97 Å) and Sm^{3+} (1.02 Å) is relatively larger than that of Hf^{4+} (0.76 Å) ion. Therefore, an enhancement in cell volume is attributed to the significant difference in ionic radii of Dy^{3+}, Sm^{3+} and Hf^{4+} cations. Further, it is observed that the crystallite size decreases while cell volume is enhanced exponentially. Yang *et al*. report a similar trend of exponential enhancement of cell volume with reduction in crystallite size for Eu doped $GdVO_4$ nanoparticles.[163] The plausible reason is described in the context of so called "Madelung model". The model suggests that an effective negative pressure can be triggered in nanosized particles due to surplus of Madelung energy which is a manifestation of both Coulomb attractive and repulsive interactions.[164, 165] Despite preserving the monoclinic phase of HfO_2, it can be inferred from the above observations that a nominal concentration of Dy^{3+} and Sm^{3+} substitute Hf^{4+} ions in the lattice.

5.2.2 Microstructural Analysis

In order to realize the shape and size of synthesized powders, FE-SEM images of D0S0, D0.5S0, D0.5S0.3 and D0.5S2 are shown in **figure 5.4.** It clearly reveals the aggregate nature of particles. Therefore, transmission electron micrograph depicted in **figure 5.5** shows partially agglomerated particles that exhibited semi-spherical shape. The estimated particle size histograms show the average particle size of ~31, 22, 18 and 16 nm

for D0S0,D0.5S0, D0.5S0.3 and D0.5S2, respectively which are sufficiently close to the crystallite size calculated using Debye-Scherrer equation.

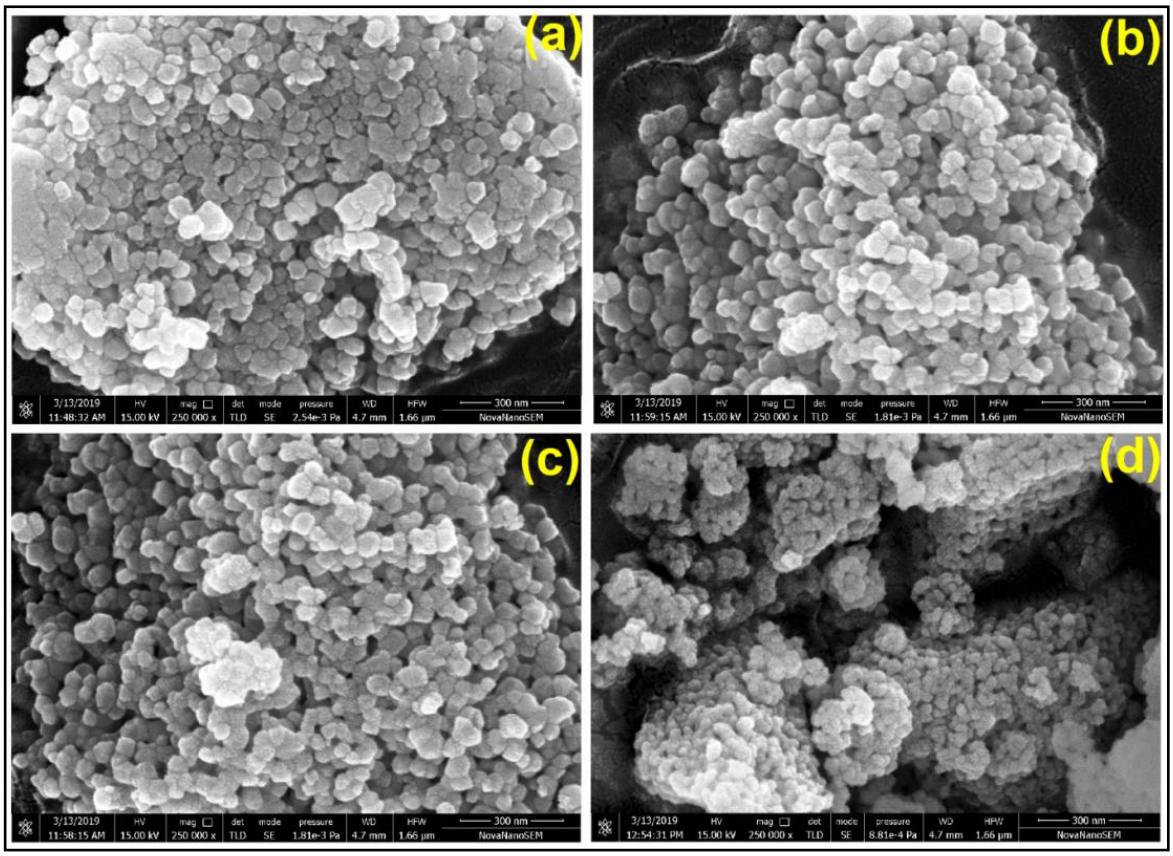

Figure 5.4 *Field emission- scanning electron micrographs (FE-SEM) of* ***(a)*** *D0S0,* ***(b)*** *D0.5S0,* ***(c)*** *D0.5S0.3 and* ***(d)*** *D0.5S2.*

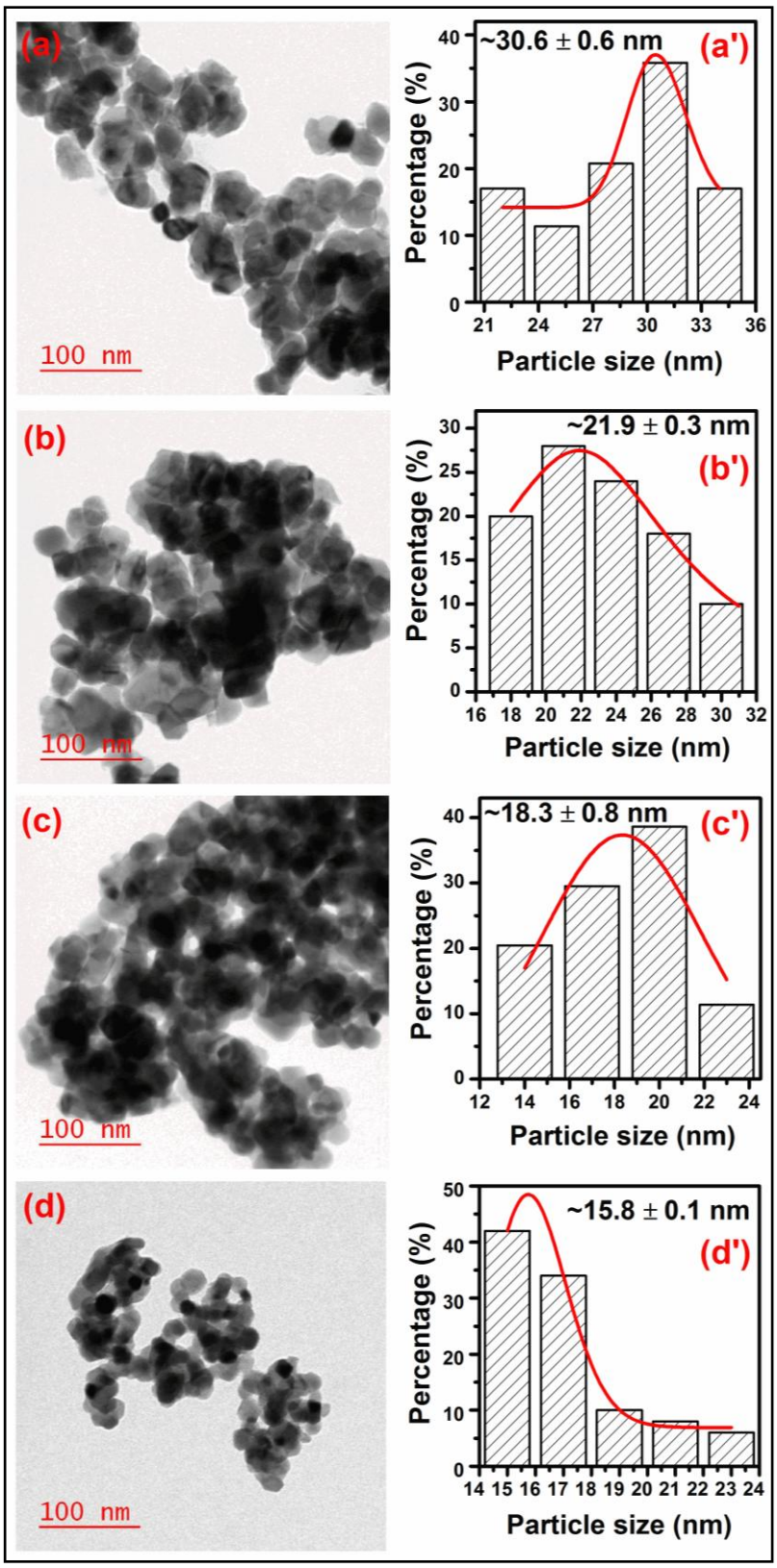

Figure 5.5 *TEM micrographs of* ***(a)*** *D0S0,* ***(b)*** *D0.5S0,* ***(c)*** *D0.5S0.3 and* ***(d)*** *D0.5S2.* ***a'-d'*** *show corresponding particle size distribution histograms.*

5.2.3 Photoluminescence properties

The photoluminescence (PL) properties of *x*Dy,*y*Sm:HfO_2 nanoparticles with different Dy and Sm concentrations are studied by means of emission, excitation and time resolved decay spectra. The excitation and emission spectra discretely correspond to the different excited and ground energy states, respectively available for electronic transitions. The excitation spectra are crucial in determining the distinct wavelengths of light that exclusively produce desired fluorescence and also useful for examining charge transfer phenomenon. The emission or excitation spectra have been measured after exposing sample by selecting the highest excitation/emission peak observed in respective PL spectrum. **Figure 5.6 (a)** depicts the excitation and emission spectra of D0.5S0 nanoparticles. The excitation spectrum observed by monitoring Dy^{3+} ion characteristic emission at 577 nm demonstrates the strongest peak centered at 352 nm emerging due to a direct excitation of electrons from $^6H_{15/2} \rightarrow {}^6P_{7/2}$ energy level. In addition, few more sharp peaks are found to be located at 367, 383 393, 425 and 448 nm assigned to various *f-f* band transitions of Dy^{3+} activator ion taking place from the ground state, $^6H_{15/2}$ to $^6P_{5/2}$, $^4F_{7/2}$, $^4I_{13/2}$, $^6G_{11/2}$ and $^4I_{15/2}$ excited energy levels, respectively. After exciting D0.5S0 nanoparticles at a wavelength of 393 nm (**figure 5.6 (a')**), the emission spectrum reveals two strong characteristic emission peaks of Dy^{3+} activator ion centered at 490 and 577 nm.[135, 166] Previously, we have obtained a similar emission spectrum for 1 at% Dy doped HfO_2 nanoparticles under an excitation wavelength of 352 nm.[167] Such characteristic emission peaks appear due to different electronic transitions occurring within distinct Dy^{3+} ion energy levels. While emission peak centered at 490 nm in blue region is ascribed to $^4F_{9/2} \rightarrow {}^6H_{15/2}$, the well separated peak located at 577 nm in yellow region

emerges primarily due to radiative relaxation of energetic electrons from metastable state, $^4F_{9/2}$ to $^6H_{13/2}$, ground state of Dy^{3+} activator ion. The emission peak occurring because of $^4F_{9/2} \rightarrow {}^6H_{13/2}$ transition is an allowed electric dipole transition which can be significantly affected by the crystal field strength around Dy^{3+} activator ion. However, the magnetic dipole transition, $^4F_{9/2} \rightarrow {}^6H_{15/2}$ is nearly insensitive to crystal field environments when Dy^{3+} ion resides at an inversion centre site with low symmetry. More often, at a site without an

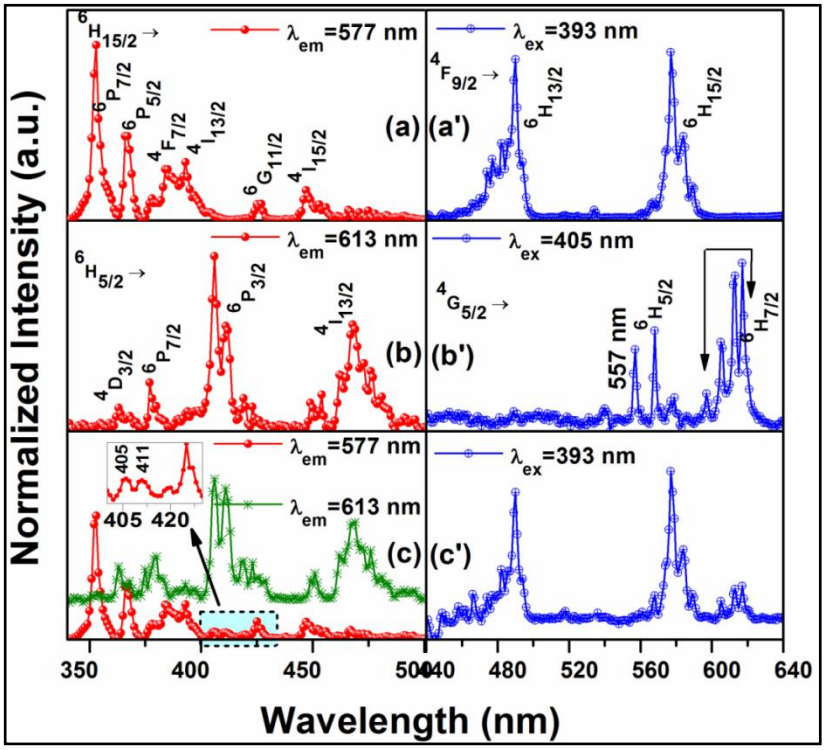

Figure 5.6 *Room temperature excitation and emission spectra of xDy,ySm:HfO_2 nanoparticles* ***(a)*** *D0.5S0 (λ_{ex}=393 nm, λ_{em}=577 nm),* ***(b)*** *D0S0.5 (λ_{ex}=405 nm, λ_{em}=613 nm) and* ***(c)*** *D0.5S2 (λ_{ex}=393 nm, λ_{em}=577 and 613 nm).*

inversion symmetry, the electric dipole transition prevails over the magnetic one.[137, 138, 167, 168] For D0S0.5 nanoparticles, the excitation spectrum is obtained in wavelength range of 340 to 500 nm after fixing the typical emission wavelength at 613 nm of Sm^{3+} ion as shown in **figure 5.6 (b)**. The excitation spectrum reveals distinguished set of intense peaks within the wavelength range of 400-420 nm (vertex at 405 nm) and 460-490 nm

(vertex at 468 nm). While the former set of excitation peaks corresponds to transition, $^6H_{5/2} \rightarrow {}^6P_{3/2}$, the latter one originates essentially due to $^6H_{5/2} \rightarrow {}^4I_{13/2}$, transition of Sm^{3+} ion. Two more excitation peaks having moderate intensity located at 362 and 378 nm in lower wavelength region are attributed to transition of electrons from ground state, $^6H_{5/2}$ to $^4D_{3/2}$ and $^6P_{7/2}$ excited states, respectively.[169, 170] It is to be noted that the excitation wavelength of 393 nm does not show any emission in D0S0.5 nanoparticles. Therefore, the emission spectrum is obtained after exciting at a wavelength of 405 nm in the wavelength range of 440-640 nm as demonstrated in **figure 5.6 (b')**. Several discrete peaks are found at 568, 577, 597, 605, 613 and 617 nm. The emission peaks located at 568 and 577 nm lying in yellow or green region arise when excited electrons relax directly from $^4G_{5/2}$ to $^6H_{5/2}$, ground state, whereas peaks in the wavelength range of 597-617 nm in near red region appear due to electronic transition, $^4G_{5/2} \rightarrow {}^6H_{5/2}$.[155] Additionally, one can notice a sharp peak at 557 nm predominantly associated to transitions occurring from different defect levels within the host, HfO_2.[82, 169, 171]

Figure 5.6 (c) compares the excitation spectra of D0.5S2 nanoparticles taken by monitoring the wavelengths of 577 and 613 nm corresponding to characteristic emissions of Dy^{3+} and Sm^{3+} ion, respectively. For λ_{em} = 577 nm, the excitation spectrum exhibits a similar set of excitation peaks to that of Dy^{3+} ion along with new small peaks within the wavelength range of 400-430 nm. With an enlarged view of 400-430 nm wavelength regime, the inset in **figure 5.6 (c)** clearly demonstrates the existence of excitation peaks such as 405 and 411 nm corresponding to Sm^{3+} ion ($^6H_{5/2} \rightarrow {}^6P_{3/2}$). It is surprising that the excitation peaks of Sm^{3+} coexist within excitation spectrum corresponding to Dy^{3+} ion. Since, the excitation peak located at 393 nm of Dy^{3+} ($^4I_{13/2}$) is sufficiently close to $^6P_{3/2}$

energy level of Sm^{3+} ion, thereby D0.5S2 nanoparticles are excited under an excitation wavelength of 393 nm. Interestingly, the emission spectrum reveals the typical set of emission peaks associated to Dy^{3+} ion together with prominent peaks in wavelength range of 600-640 nm attributed to Sm^{3+} activator ion. Such a coexistence of characteristic emission peaks corresponding to Dy^{3+} and Sm^{3+} ion is only possible if there is transfer of excited electrons between energy levels of Dy^{3+} and Sm^{3+} active ions. Villabona-Leal *et al.* report the enhancement in luminescence intensity due to an energy transfer process occurring among Eu^{3+} and Gd^{3+} active ions codoped in a similar system like ZrO_2.[172]

After exciting at 393 nm, the emission spectra of *x*Dy,*y*Sm:HfO_2 are shown in **figure 5.7**. For D0.5S0 sample, the emission spectrum consists of two prominent peaks observed at 490 and 577 nm. Keeping Dy concentration constant at 0.5 at%, with increase in Sm concentration from 0.01 to 0.05 at%, along with strong emissions corresponding toDy^{3+} ion, a set of emission peaks are observed at 605, 613 and 617 nm (see right panel of **figure 5.7**). Interestingly, these emission peaks become well resolved, distinguishable and more prominent with increasing Sm concentration upto 2 at%. These set of emission peaks in near red region (605-617 nm) are result of electronic transition taking place from $^4G_{5/2}$ to $^6H_{7/2}$, ground state of Sm^{3+} ion. The distinct character of emission peaks corresponding to Sm^{3+} ion is indicative of Stark splitting under the crystalline field of host lattice. The direct transition, $^4G_{5/2} \rightarrow {}^6H_{7/2}$ includes contributions from both the magnetically and electrically allowed dipole transitions.[155, 173, 174] Therefore, it can be accomplished that in Dy and Sm codoped HfO_2, Dy^{3+} ions are capable of sensitizing the photoluminescence properties of Sm^{3+} activator ion through an efficient mutual interaction rendering improved optical properties.

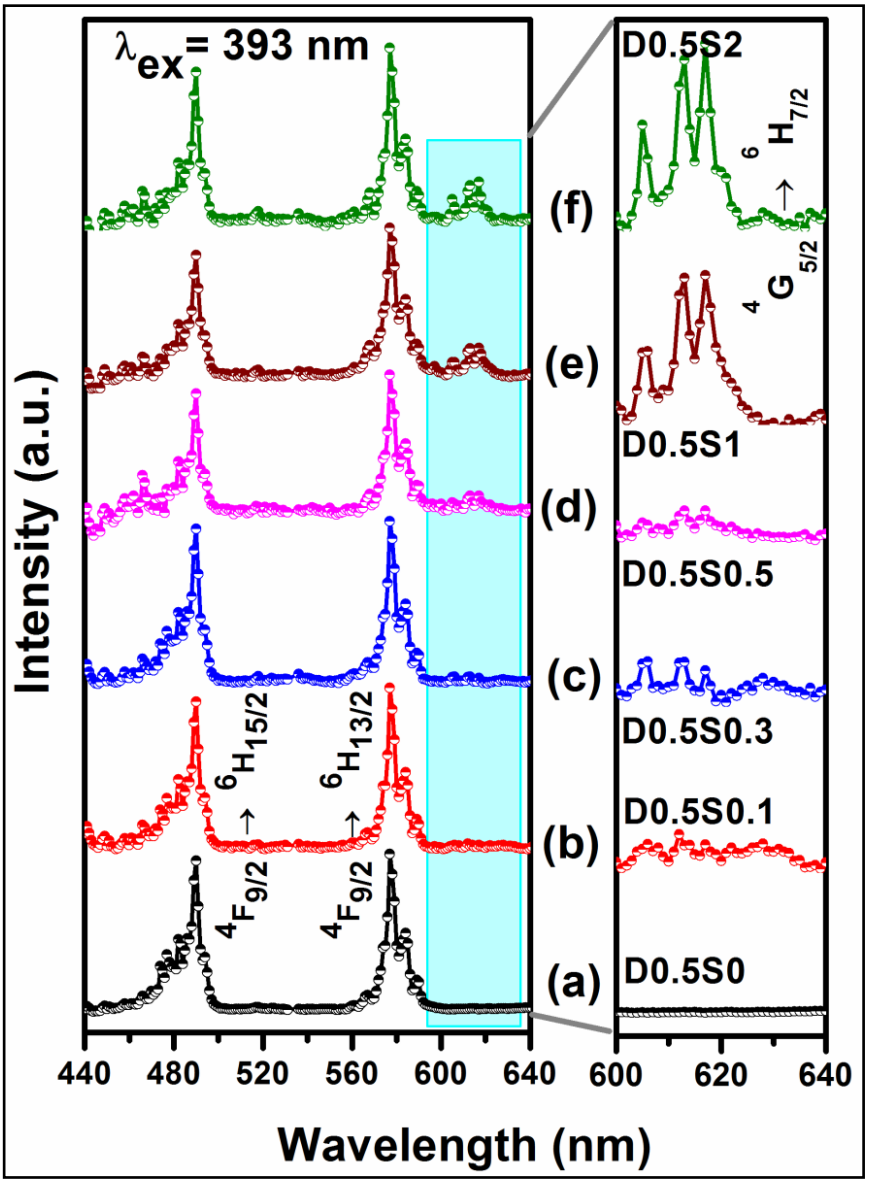

Figure 5.7 *Room temperature PL emission spectra of xDy,ySm:HfO_2 nanoparticles obtained under an excitation wavelength of 393 nm. In right panel, an enlarged view of emission peaks within the wavelength range of 600-640 nm is shown. (**a-f** correspond to D0.5S0, D0.5S0.1, D0.5S0.3, D0.5S0.5, D0.5S1, and D0.5S2, respectively).*

5.2.4 Time Resolved Decay Curves

The presence of possible inter-system energy transfer phenomenon occurring within Dy^{3+} and Sm^{3+} coactivated HfO_2 nanoparticles is studied in the context of time resolved luminescence decay curves. **Figure 5.8 (a-f)** show the luminescence decay curves of

*x*Dy,*y*Sm:HfO_2 nanoparticles as a function of Sm concentration with constant Dy concentration (0.5 at%). The time resolved decay curves are collected in millisecond time domain after exciting at a wavelength of 393 nm while monitoring emission peak at 577 nm of Dy^{3+} ion. Apparently, the luminescence decay lifetime could be affected by the presence of Dy^{3+} and/or Sm^{3+} ions which may not be evenly distributed in HfO_2 lattice. As

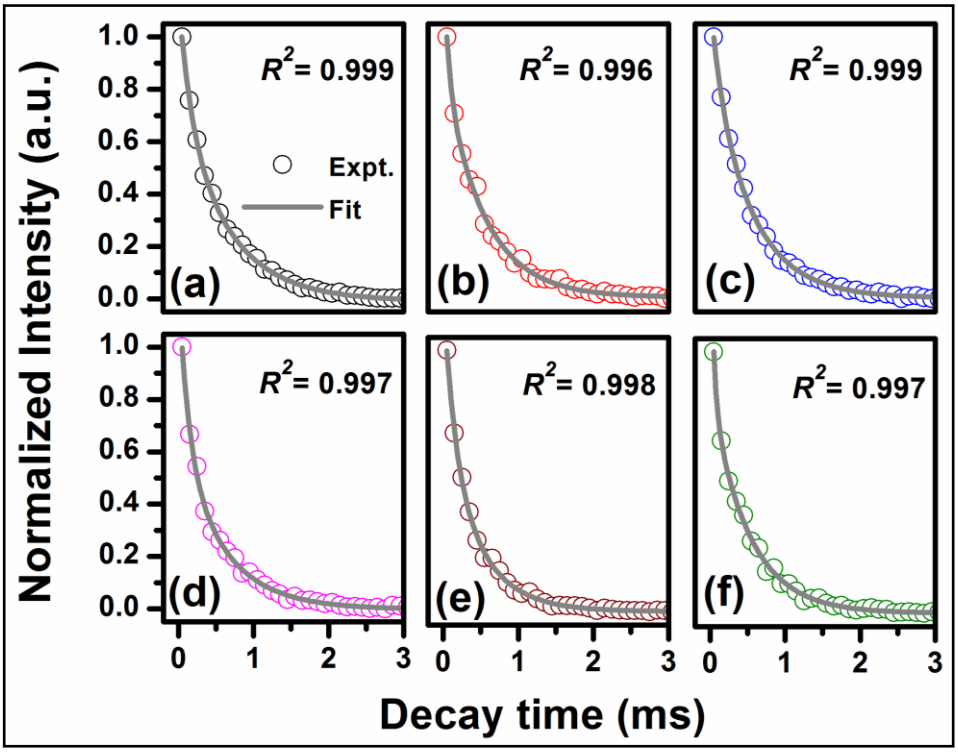

Figure 5.8 *Time resolved luminescence decay curves of emission peak at 577 nm corresponding to Dy^{3+} ion monitored after exciting at a wavelength of 393 nm for different Sm concentrations. (**a-f** correspond to D0.5S0, D0.5S0.1, D0.5S0.3, D0.5S0.5, D0.5S1, and D0.5S2, respectively).*

a result, the different local environments around RE active ions can give rise to different luminescence decay behavior.[175, 176] In general, luminescence decay curve is fitted using single-exponential function given as $I(t) = I_0 e^{-t/\tau}$ where I_0 and I are luminescence

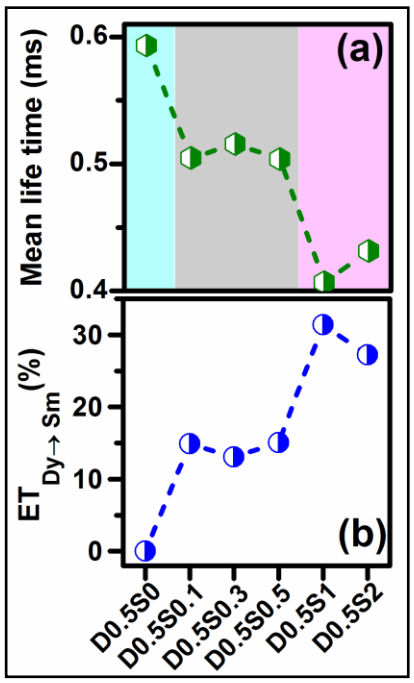

Figure 5.9 *Variation in* ***(a)*** *mean lifetime and* ***(b)*** *efficiency of energy transfer from* Dy^{3+} *to* Sm^{3+} *ion as a function of Sm concentration.*

intensity measured at 0 and at an instant, *t*, respectively and τ is the resulted lifetime. For Dy and Sm codoped HfO_2, in contrast to single exponential fitting, a double-exponential function, $I(t) = I_1 e^{-t/\tau_1} + I_2 e^{-t/\tau_2}$ fits well with the experimental data. The parameters, *I* is intensity corresponding to Dy^{3+} ions, I_1 and I_2 are respective constants, τ_1 and τ_2 are known as characteristic lifetimes denoted as fast and slow decay components.[176] The calculated coefficient of determination (COD), R^2 values are found to be ~0.995 and ~0.999 for single and double exponential function fits, respectively. Hence, we have adopted a double-exponential function to fit all decay curves. After fitting experimental data, the extracted parameters like I_1, I_2, τ_1 and τ_2 have been utilized to estimate the mean lifetime (τ_m) through following relation.[175]

$$\tau_m = (I_1\tau_1^2 + I_2\tau_2^2) / (I_1\tau_1 + I_2\tau_2)$$

The mean lifetimes are found to be in the range of ~0.59 to 0.43 ms for *x*Dy,*y*Sm:HfO_2 shown in **figure 5.9 (a)**. It is evident that HfO_2 nanoparticles doped with only Dy^{3+} ion show longer lifetime value of ~0.6 ms. The estimated τ_m value agrees well with the reported value for Dy^{3+} ion characteristic emission at 577 nm.[176, 177] However, after doping 0.1 at% of Sm, keeping Dy concentration fixed, τ_m decreases to ~0.5 ms which remains almost constant upto 0.5 at% of Sm. At 1 and 2 at% of Sm concentration, τ_m further shortens and reaches ~0.4 ms showing ~30% reduction in τ_m value. This fact indicates a more rapid decay of Dy^{3+} ions with increasing Sm concentration which could be due to non-radiative transfer of energetic electrons from Dy^{3+} to Sm^{3+} active ions. Considering the existence of an energy exchange between Dy^{3+} and Sm^{3+} active ions, the efficiency of energy transfer (ET) is related to activator ion lifetime expressed as follows.[178]

$$(ET)_{Dy\rightarrow Sm} = 1 - (\tau_{Dy}'/\tau_{Dy})$$

where τ_{Dy}' and τ_{Dy} are lifetimes of sensitizer i.e. Dy^{3+} ions in presence and absence of Sm^{3+} ions, respectively. The variation in calculated efficiency of energy transfer from Dy^{3+} to Sm^{3+} ions with increasing Sm concentration depicted in **figure 5.9 (b)** shows that $(ET)_{Dy\rightarrow Sm}$ enhances with increasing Sm concentration. A maximum of ~30% energy is being transferred from Dy^{3+} to Sm^{3+} ions when Sm concentration reaches upto 2 at%.

In order to realize Dy^{3+} and Sm^{3+} interaction process, we discuss the energy transfer mechanism after calculating the distance between two neighboring active ions pairs such as $Dy^{3+} - Dy^{3+}$, $Dy^{3+} - Sm^{3+}$ or $Sm^{3+} - Sm^{3+}$ using following expression.[179]

$$R = (M_{HfO_2}/N_A \rho C)^{1/3}$$

Sample	**Average Distance, *R* (Å)**		
	Dy^{3+}–Dy^{3+}	**Dy^{3+}–Sm^{3+}**	**Sm^{3+}–Sm^{3+}**
D0.5S0	19.18	-	-
D0.5S0.1	19.18	18.06	32.63
D0.5S0.3	19.18	16.43	22.71
D0.5S0.5	19.18	15.26	19.18
D0.5S1	19.18	13.36	15.25
D0.5S2	19.18	11.27	12.15

Table 5.2 *The average distance (R) between different neighboring ion pairs for varying Sm concentration in HfO_2 nanoparticles.*

where *R* is the distance between two adjacent active ions, *C* is total concentration of Dy^{3+} and/or Sm^{3+} ions, N_A is Avogadro number, M_{HfO_2} is molecular weight and ρ is the density (9.7 g/cm^3) of of host HfO_2, respectively. The estimated average values of *R* at different concentrations of Sm are listed in **Table 5.2**. The average *R* value varies from ~18.1 to 11.3 and ~32.6 to 12.2 Å for Dy^{3+} − Sm^{3+} and Sm^{3+} − Sm^{3+} ion pairs, respectively. On the basis of above results, it can be inferred that at low Sm concentrations (0.1-0.5 at%), Sm^{3+} ions are located far from adjacent Dy^{3+} or Sm^{3+} active ion and sparsely distributed in HfO_2 lattice acting as isolated luminescent centers. As a consequence, a few excited electrons transfer from sensitizer Dy^{3+} to Sm^{3+} ion diminishing the sensitizer lifetime appreciably. After increasing Sm concentration upto 2 at%, *R* value further decreases and activator ions such as Dy^{3+} and Sm^{3+} form pairs which essentially evoke transfer of more and more electrons from sensitizer to Sm active ions enhancing photoluminescence properties. Further, in order to determine the process by which the energy is being transferred from sensitizer to activator ion, two processes/mechanisms are suggested (i) exchange

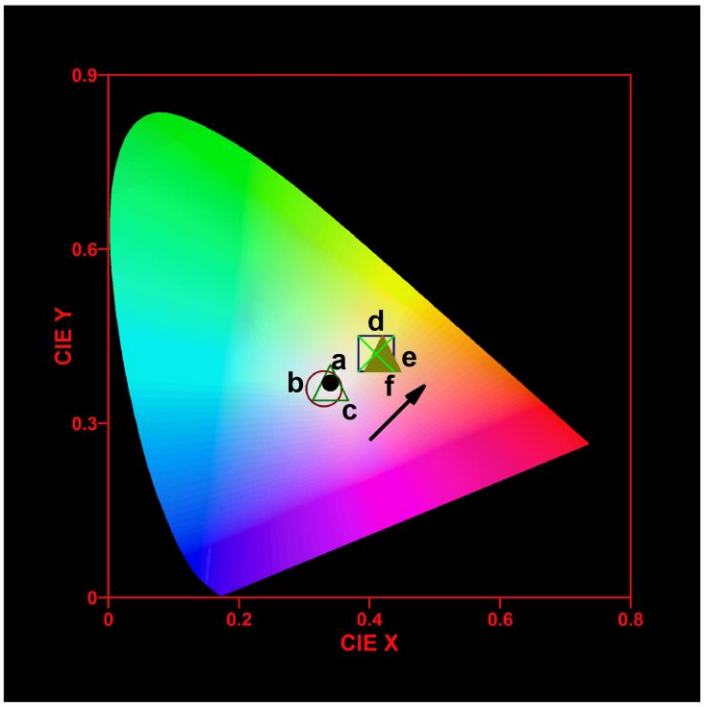

Figure 5.10 *CIE chromaticity diagram of xDy,ySm:HfO_2 nanoparticles after exciting with a wavelength of 393 nm. (**a-f** correspond to D0.5S0, D0.5S0.1, D0.5S0.3, D0.5S0.5, D0.5S1, and D0.5S2, respectively)*

interaction and (ii) multipolar interaction process.[180] Depending on the critical distance between sensitizer and activator ion, one of two processes become dominant and contribute in energy transfer mechanism. It is established that at a critical distance below 5 - 6 Å, the energy is transferred predominantly through an exchange interaction process.[179, 180] However, in our case, the calculated *R* values are well above 6 Å. This reveals that multipolar interaction prevails over exchange interaction type mechanism and governs the existing energy transfer process from sensitizer Dy^{3+} to Sm^{3+} active ions in HfO_2 nanoparticles. A two dimensional Commission Internationale de I'Eclairage 1931 (CIE xy) chromaticity diagram for *x*Dy,*y*Sm:HfO_2 nanoparticleswith varying Sm concentration obtained after exciting with wavelength of 393 nm is shown in **figure 5.10**. The CIE coordinates are estimated as (0.35,0.37), (0.33,0.36), (0.34,0.37), (0.41,0.42), (0.42,0.42)

and (0.41,0.41) for *x*Dy,*y*Sm:HfO_2, respectively. It can be noted that at low concentrations, *x*=0.5 and *y*=0.1 and 0.3 at %, CIE coordinates are almost similar rendering near white light emission. However, at higher concentration of Sm, HfO_2 produces purplish light color due to significant contribution from Sm^{3+} ion characteristic emissions emerging along with Dy^{3+} emission peaks.

5.2.5 Energy Band Diagram

On the basis of excitation, emission and time resolved luminescence decay spectra, we, herein suggest a simplified schematic energy level diagram to realize different processes involved in Dy^{3+} and Sm^{3+} coactivated HfO_2 nanoparticles (**figure 5.11**). The respective energy levels of Dy^{3+} ion such as $^6H_{11/2}$, $^6H_{13/2}$, $^6H_{15/2}$, $^4F_{9/2}$, $^4I_{13/2}$, $^4F_{7/2}$, $^6P_{5/2}$, $^6P_{7/2}$, $^6P_{3/2}$ and $^4I_{9/2}$ and$^6P_{3/2}$, $^4I_{13/2}$, $^4G_{5/2}$, $^6H_{5/2}$, $^6H_{5/2}$, $^6H_{5/2}$ corresponding to Sm^{3+} ion are labeled. Due to wide band gap (~5.7 eV) of host, HfO_2, electrons can only reach to specific energy levels of activator ions after exciting with a wavelength of 393 nm i.e. lower energy. Upon excitation under a wavelength of 393 nm, electrons at ground state, $^6H_{15/2}$, absorb the pumping energy and get populated at higher energy level, $^4I_{13/2}$ of Dy^{3+} ion. Afterwards, excited electrons follow a multistep nonradiative relaxation to a metastable state, $^4F_{9/2}$ and while finally arriving at ground states such as $^6H_{15/2}$ and $^6H_{13/2}$ induce intense emissions at 490 and 577 nm corresponding to Dy^{3+}. However, in the presence of Sm^{3+} ion, characteristic emissions due to electronic transitions from excited state, $^4G_{5/2}$ to ground state of Sm^{3+}, $^6H_{7/2}$ produce a set of emission peaks at 600-640 nm along with Dy^{3+} emissions. These emission peaks become stronger as the efficiency of energy transfer enhances considerably with increasing Sm concentration in HfO_2.

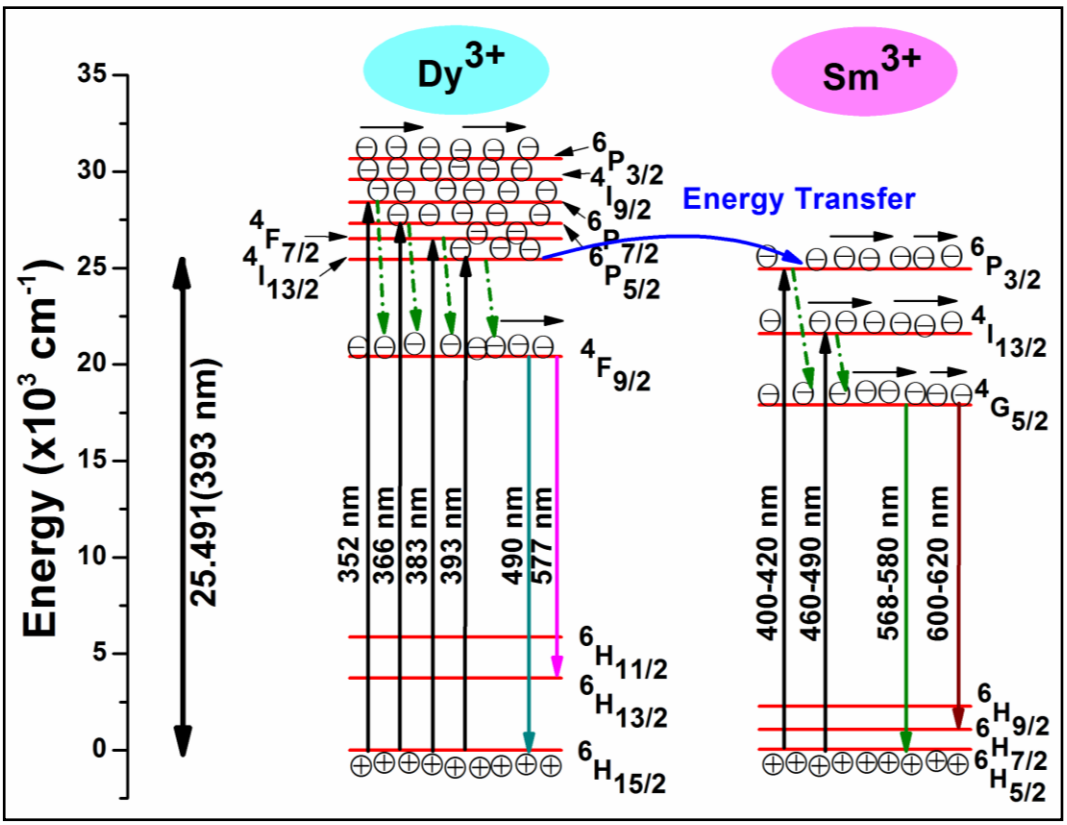

Figure 5.11 *A simplified schematic energy level diagram demonstrating different emission, excitation processes and energy transfer in Dy and Sm codoped HfO_2 nanoparticles.*

Such an observation of simultaneous emissions from Dy^{3+} and Sm^{3+} ion is realized because of significant energy exchange through multipolar interaction between different energy levels of both activator ions. Since excited energy level, $^4I_{13/2}$ of sensitizer Dy^{3+} and $^6P_{3/2}$ corresponding to Sm^{3+} active ion lie within close regime, electrons populated at these levels can reciprocate easily to produce characteristic emissions. The higher levels of sensitizer Dy^{3+} ion such as $^6P_{7/2}$ and $^6P_{5/2}$ do not participate in such energy exchange process due to appreciably large energy separation between Dy^{3+} excited and Sm^{3+} emission levels. Therefore, it can be concluded that in Dy^{3+} and Sm^{3+} coactivated HfO_2 nanoparticles, the energy transfer from Dy^{3+} is possible only between excited levels lying in close proximity of Sm^{3+} energy levels which can remarkably tune the photoluminescence

properties furnishing desired optical performance. Looking at promising luminescence properties, we have exploited the synthesized nanoparticles for application in latent fingerprint imaging.

5.2.6 Application in Latent Fingerprint Imaging

Using Dy^{3+} and Sm^{3+} coactivated HfO_2 nanoparticles, we demonstrate a proof of concept for detecting latent fingerprints on different object surfaces. In general, human finger skin is covered with lipid substances insoluble in water and leave practically invisible marks upon object surfaces when touched.[181] In practice, a good contrast between fingerprint impression and substrate background is sought after for LFPs development with highly detailed and distinct features for an individual identification. In addition, a better adherence of labeling powder with ridges present in fingerprint patterns is a prerequisite and equally important.[182, 183] For an effective, fast, and hassle free development of LFPs, a step by step procedure is followed as depicted schematically in **figure 5.12**. First, the left hand thumb finger of donor to be marked is washed properly with soap solution and dried under hot air blower. LFPs are obtained by gently pressing thumb over thoroughly clean surface of different objects such as transparent glass, aluminum foil, colored plastic sheets, and stainless steel. The synthesized Dy and Sm codoped HfO_2 has been utilized as proposed dusting or labeling powder and sprinkled onto object surface containing LFPs. Any excess amount of powder is then blown-off which revealed undistinguished and vague fingerprint under bright light environment. However, under long UV light of 395 nm irradiation, LFPs become completely visible demonstrating a well defined and distinguishable fingerprint ridge pattern. Finally, a digital camera was

used to capture the photographs of LFPs developed after sprinkling Dy and Sm codoped HfO_2 powder.

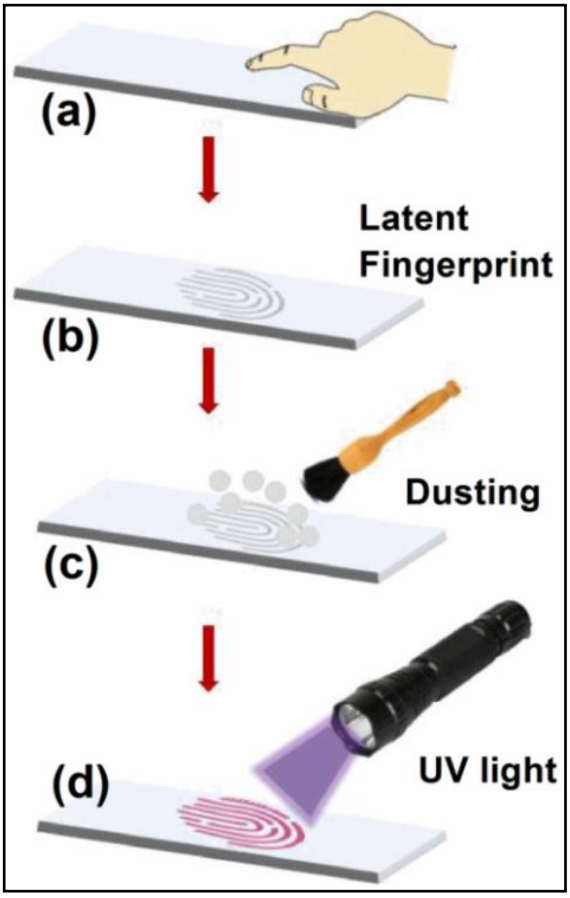

Figure 5.12 *An illustration of the process flow adopted for developing latent fingerprint using Dy and Sm coactivated HfO_2 powders* ***(a)*** *printing finger impression on a substrate,* ***(b)*** *latent fingerprint,* ***(c)*** *dusting using synthesized powders and* ***(d)*** *exposure under ultra-violet (UV) light of 395 nm.*

Figure 5.13 (a), (b) and (c) compares fresh LFPs impressions onto transparent glass, LFPs after D0.5S2 powder labeling in bright light condition and under 395 nm UV illumination, respectively. The fresh fingerprint impression on glass substrate is completely invisible to naked eye. However, in bright light environment (**figure 5.13 (b)**), the stained

latent fingerprint appears ambiguous to naked eyes and it is difficult to realize the whole fingerprint impression distinctively. Interestingly, under irradiation using a handheld 395 nm UV light (**figure 5.13(c)**), a complete fingerprint pattern is clearly recognized with discrete ridge shaped pattern. This observation confirms a good adsorption efficiency of Dy^{3+} and Sm^{3+} coactivated HfO_2 nanoparticles with ridges of fingerprint on a glass surface.

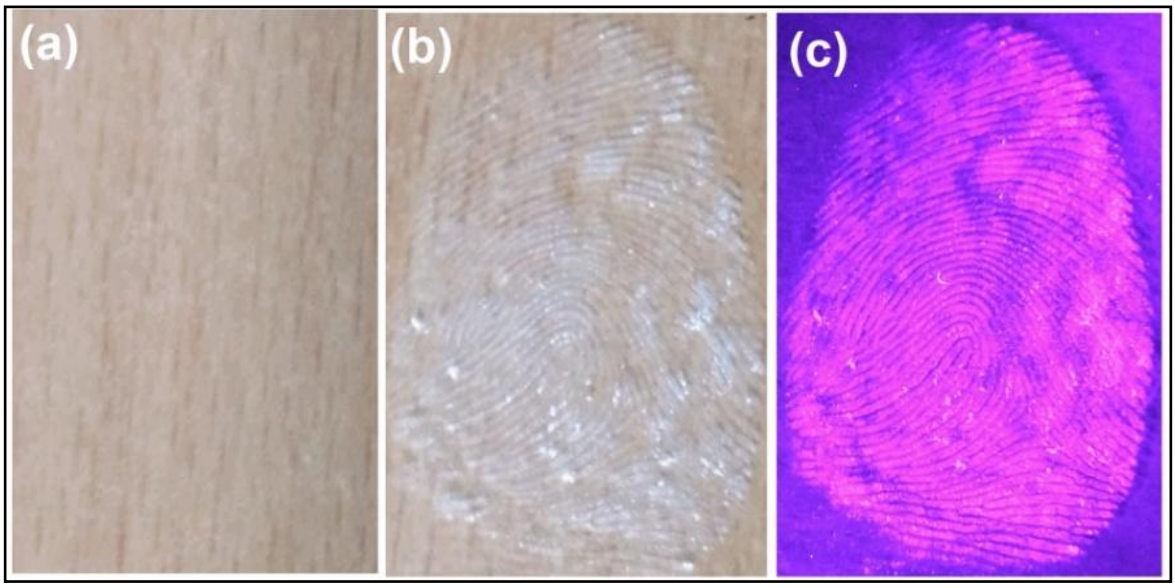

Figure 5.13 *An illustrative comparison of developed latent fingerprints marked over transparent glass surface sprinkled with Dy^{3+} and Sm^{3+} coactivated HfO_2 nanoparticles* ***(a)*** *LFP over glass* ***(b)*** *LFP after dusting in bright light environment and* ***(b)*** *under illumination of UV light (395 nm).*

To determine the viability and developing selectivity, we investigate the adsorption capability and performance of Dy^{3+} and Sm^{3+} coactivated HfO_2 nanoparticles labeled latent fingerprints marked onto common household object surfaces such as transparent glass, plastic sheet and stainless steel etc. **Figure 5.14 (a-f)** show LFPs imaging developed using D0.5S2 powder and then observed under illumination of 395 UV light upon aluminum foil,

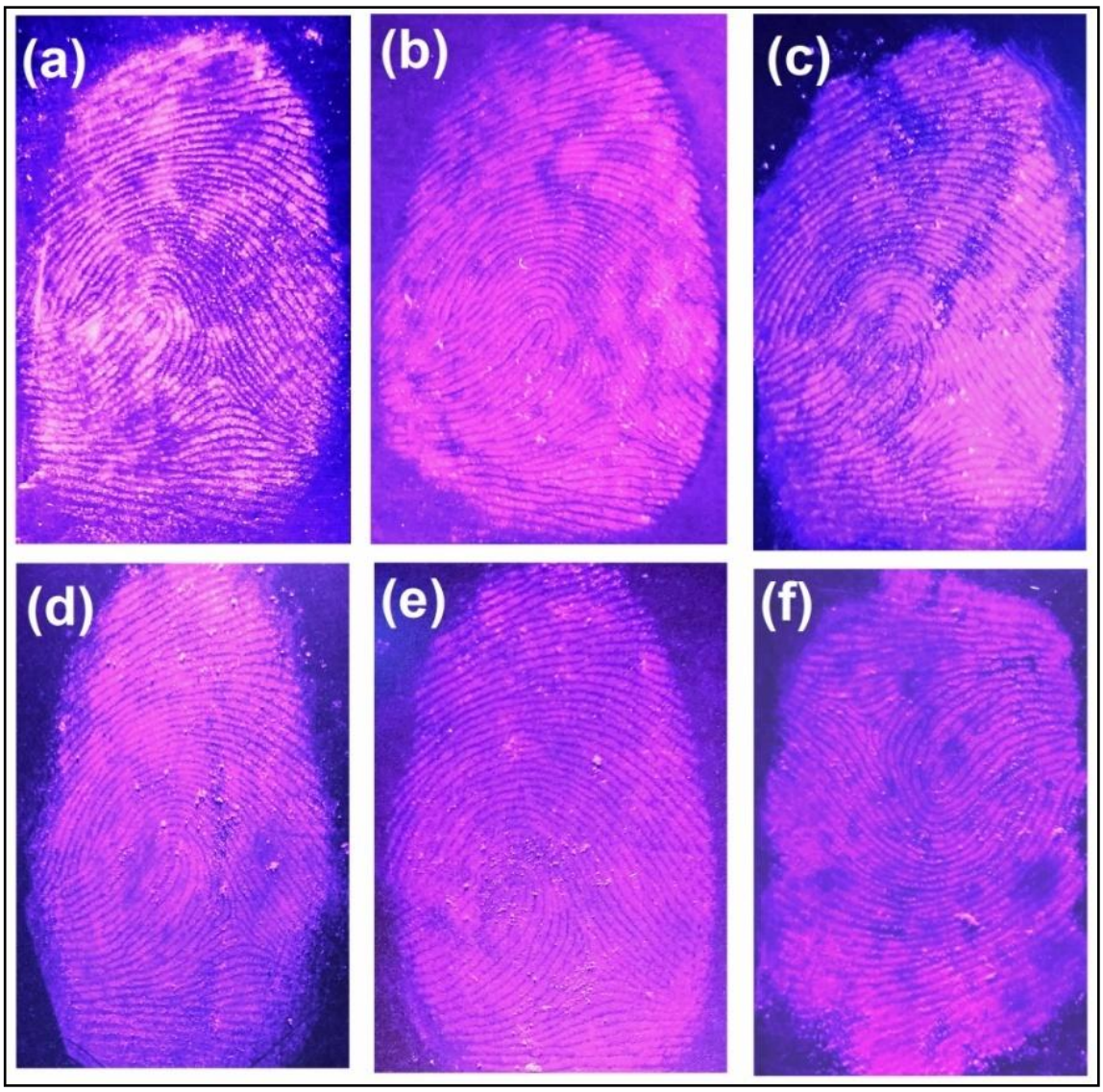

Figure 5.14 *The optical images of latent fingerprints developed using Dy^{3+} and Sm^{3+} coactivated HfO_2 nanophosphors and detected under 395 nm UV irradiation:* ***(a)*** *aluminum foil,* ***(b)*** *transparent glass,* ***(c)*** *black colored glass,* ***(d)*** *wine colored,* ***(e)*** *red colored plastic sheets and* ***(f)*** *stainless steel.*

transparent glass, black colored glass, wine and red colored plastic sheets and stainless steel, respectively. All LFPs images developed over different surfaces reveal lucid and bright fingerprint impressions containing a full ridge flow and pattern. A sufficiently distinguished and well defined appearance of developed LFPs with an explicit ridge pattern

demonstrate a high contrast with background and excellent resolution of imaged fingerprints. In order to achieve a high developing selectivity of latent fingerprints, an enough color contrast between luminescent powders and background is desirable.[184]

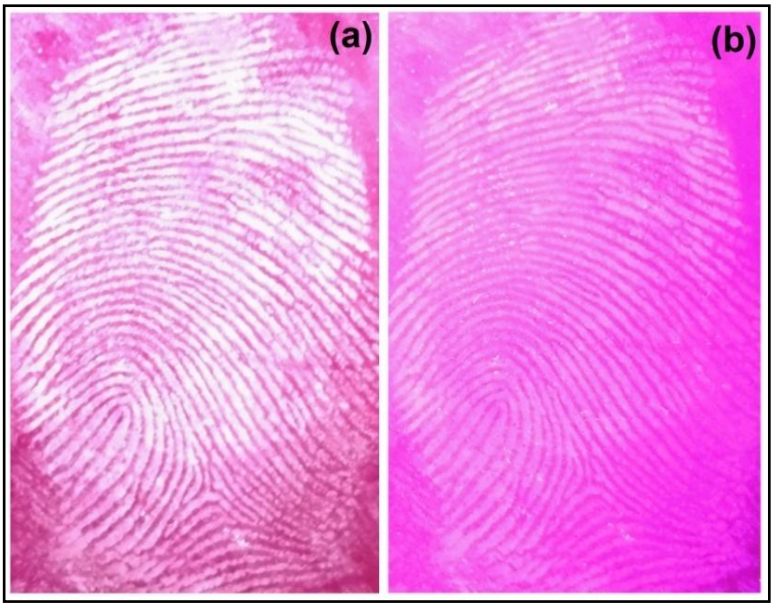

Figure 5.15 *A comparison of LFPs images developed using D0.5S2 powder over purplish colored surface recorded* ***(a)*** *in bright light environment and* ***(b)*** *under 395 nm UV irradiation.*

Nevertheless, latent fingerprints impressions labeled with Dy^{3+} and Sm^{3+} coactivated HfO_2 nanoparticles under 395 nm UV exposure examined over various object surfaces maintained an appropriate resolution, less interference with background and suitable color contrast for extracting minute details to identify an individual. Further, we have examined the purplish colored surface background interference with developed LFPs (**figure 5.15**). The result indicates minor background interference with an acceptable resolution revealing minute characteristic details. In present investigations on LFPs recognition, all fingerprint impressions formed onto object surfaces are enriched essentially with sweat or sebum. It is

known that adsorption efficiency of powders onto fingerprint is dependent on adhesive bond formation between powder particles and ridges of fingerprint.[185, 186] The luminescent dusting powders constituting of smaller particle size provide a better degree of adhesion with most of the object surfaces. The mechanical adhesion process is explained in terms of pressure deficiency produced among powder particle and a ridge within fingerprint.[181] Owing to nanorange particle size (~15 nm) of Dy^{3+} and Sm^{3+} coactivated HfO_2 nanoparticles, the synthesized luminescent powder offers superior adsorption capability for developing LFPs.

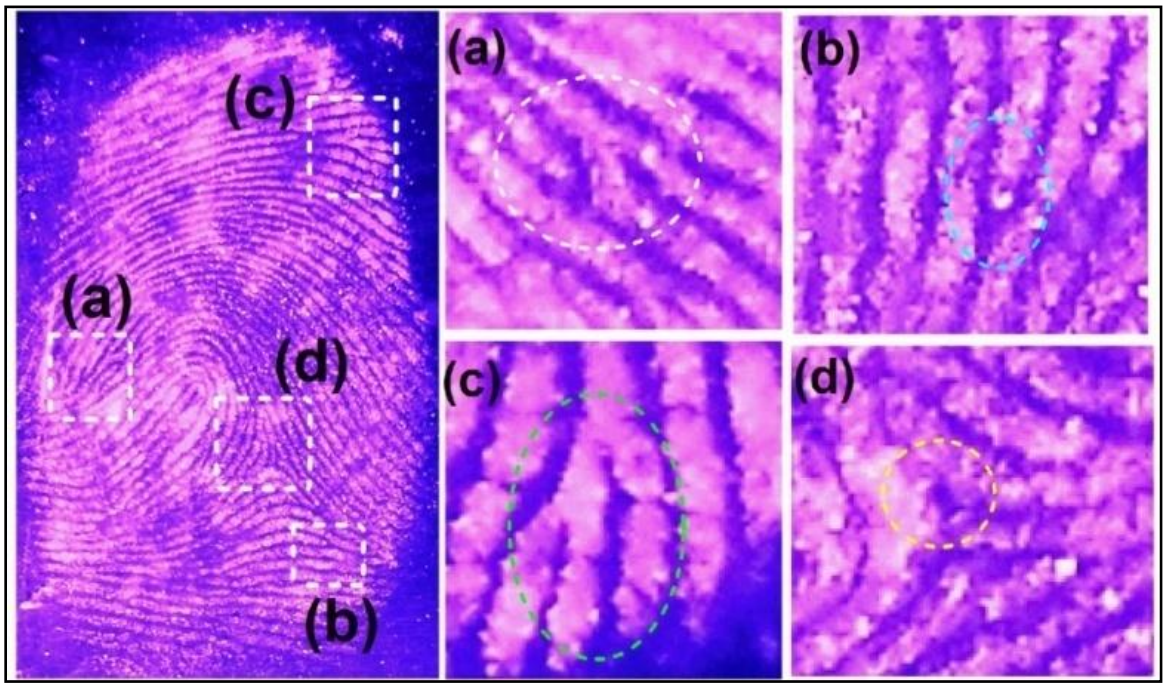

Figure 5.16 *The developed latent fingerprint over aluminum foil labeled by Dy^{3+} and Sm^{3+} coactivated HfO_2 nanophosphors showing selected magnified regions with third-level details distinctive to an individual such as (a) termination along with single bifurcation, (b) termination of a ridge, (c) a crucial double bifurcation and (d) an enclosure.*

Figure 5.16 depicts a typical fingerprint on aluminum foil substrate labeled with Dy^{3+} and Sm^{3+} coactivated HfO_2 nanoparticles along with four highlighted enlarged regions of investigation. The specified sections, **figure 5.16 (a-d)** demonstrate the existence of a termination along with single bifurcation, termination of a ridge, a crucial double bifurcation and an enclosure, respectively. Such third-level details of a fingerprint remain distinguishable even after magnification. These distinct features are very crucial and eventually utilized for identifying an individual easily.[187, 188] In consideration to above observations, one can conclude that Dy^{3+} and Sm^{3+} coactivated HfO_2 nanoparticles is proficient at developing clear latent fingerprints over different household object surfaces. Under 395 nm UV irradiation, Dy and Sm codoped HfO_2 developed LFPs show full ridge flow and pattern with characteristic features comparable to LFPs labeled with $NaYF_4$:Yb,Er; YVO_4:Eu and $LaPO_4$:Ce,Tb powders imaged under 980 nm NIR or 254 nm deep UV irradiation, respectively. A fine nature of prepared nanoparticles guarantees a high stability against fingerprints marked onto variable surfaces. Thereby, the developed fingerprints comprise of well resolved and comprehensible minutiae details e.g. ridge termination, bifurcations and enclosures useful for hassle-free individual identification process. Since Dy^{3+} and Sm^{3+} coactivated HfO_2 nanoparticles are non-hazardous, it is more appropriate to be employed in LFPs imaging with good developing selectivity and sensitivity.

5.3 Conclusions

To summarize, after codoping Dy and Sm upto the total concentration of 13 at%, we successfully demonstrated the stabilization of high temperature cubic phase of HfO_2 at room temperature. The robustness of luminescent Dy and Sm codoped HfO_2 nanoparticles

was investigated as a prospective dusting powder for an effective development of latent fingerprints. Dy and Sm codoped HfO_2 having low dopant concentration showed only the monoclinic phase of HfO_2 as observed by XRD, Le-Bail profile fitting and selected area electron diffraction pattern. With increasing Sm concentration, the crystallite size decreased significantly from ~25 to ~10 nm leading to an exponential enhancement of cell volume essentially due to negative pressure effect manifested by nanosize characteristic of the particles. Detailed photoluminescence studies demonstrated that under an excitation wavelength of 393 nm, Dy and Sm codoped HfO_2 revealed prominent emission peaks in blue, yellow and near red spectral regions producing purplish colored light. A systematic study of the time resolved decay spectra confirmed the existence of an energy transfer from Dy^{3+} to Sm^{3+} ions occurring via a multipolar interaction which eventually induced excellent emissions from Dy and Sm coactivated HfO_2. On the basis of excitation and emission spectra, we proposed an energy band diagram to perceive different allowed electronic transitions. Dy and Sm coactivated HfO_2 nanophosphors were successfully applied as a versatile luminescent powder for selective LFPs imaging. The developed LFPs onto several surfaces including aluminum foil, float glass, black colored glass, wine and red colored plastic sheets and stainless steel exhibited third-level details, good background contrast, selectivity and resolution. The effectiveness of non-hazardous luminescent powders in detecting LFPs was realized due to nanosize nature of particles with improved adsorption capability.